J Mater Sci: Mater Electron **(2024) 35:676**

Influence of vanadium and dysprosium co-doping on phase stability, microstructure, and electrical properties of Bi_2O_3

Ahmed H. Ibrahim[1,*], Yehia M. Abbas[1], Marwa H. Ali[1], H. A. Ayoub[1], and Mustafa Aldoori[1,2]

[1] *Materials Science Laboratory, Physics Department, Faculty of Science, Suez Canal University, Ismailia 41522, Egypt*
[2] *Ministry of Higher Education and Scientific Research, Aliraqia University, Baghdad 10011, Iraq*

Received: 21 January 2024
Accepted: 12 March 2024
Published online: 1 April 2024

ABSTRACT

Herein, we report the synthesis of Dy–V co-doped Bi_2O_3 ceramics using the solid–state processing technique under atmospheric conditions. The X-ray diffraction (XRD) patterns demonstrate the stability of the cubic fluorite δ-Bi_2O_3 in the V-rich ceramics. However, in Dy-rich ceramics, a mixture of phases, including α and δ, gradually diminishes with increased mutual dopant concentrations, suggesting a transition to the single fcc δ-phase with Fm-3 m space group. According to the Rietveld analysis and electron density representation, it is evident that there are no impure peaks present in α-Bi_2O_3, which highlights the clear transition to the δ-phase polymorphs. The DTA curves for samples M4 and M7 display a distinct endothermic peak at temperatures around 724.5 and 744.5 °C, indicating a phase transition from the monoclinic α-phase to the cubic δ-phase. These peaks are also attributed to an order-disorder transition (ODT). The FESEM micrographs consistently revealed the existence of irregular and aggregated grains, with an average grain size ranging from 0.80 to 5.57 μm. The level of aggregation became more apparent with the escalation of Dy^{3+} doping, as opposed to the 5–20 wt% V loading. Moreover, the as-sintered pellets M2 demonstrated the absence of any pore formation compared to other samples, confirming a remarkably high degree of densification. As a result, the as-sintered pellets have a low level of void space, with an apparent porosity of no more than 2.5%. Based on the conductivity measurements and electrochemical impedance spectroscopy (EIS), $Bi_{0.85}V_{0.10}Dy_{0.05}O_{1.5}$ exhibits the highest electrical conductivity of 0.965 $(\Omega\ cm)^{-1}$ and an optimal activation energy of 0.537 eV at 627 °C compared to other prepared compositions. This remarkable performance is attributed to the high polarizability and mixed valence cations, especially in V^{5+}-rich ceramics, compared to the Dy^{3+}-rich compositions with a reduced conductivity of 0.010 to 0.097 $(\Omega\ cm)^{-1}$. The Nyquist plots indicate that impedance decreases with vanadium doping increases until

Address correspondence to E-mail: ahmed_abdel-hamid@science.suez.edu.eg

E-mail Addresses: Ymabbas@yahoo.com; Marwa_hussien@science.suez.edu.eg; hyamayoub@yahoo.com; Mn_200422@yahoo.com

https://doi.org/10.1007/s10854-024-12371-4

it reaches $Bi_{0.85}V_{0.10}Dy_{0.05}O_{1.5}$. Higher Dy^{3+} content increases impedance, leading to lower cell performance. The typical composition can be a solid electrolyte in SOFCs operating at moderate temperatures.

1 Introduction

The oxygen-defective ceramic material, δ-Bi_2O_3, is rapidly gaining prominence in oxide-based technological advancements owing to its high oxygen-ion conductivity. Researchers find Bismuth (Bi) extremely appealing for its exceptional charge mobility (˃ 100 m^2 /(V s), at 4 K), which leads to high electrical conductivity and relative magnetoresistance [1]. It boasts a wide range of applications in sensor technology [1], making it an essential component in this field. Additionally, it is known for its exceptional environmental friendliness, having one of the lowest toxicity levels among all the heavy elements. These δ-Bi_2O_3-based ceramics are an excellent option as a solid electrolyte in high-temperature fuel cells, particularly Solid Oxide Fuel Cells (SOFCs). These fuel cells are known for their high efficiency and eco-friendliness and require a reliable and robust solid electrolyte to function optimally. In a standard SOFC setup, a single cell is made up of three distinct, dense, and continuous parts: the anode, which helps oxidize gaseous fuel; the cathode, which helps reduce O_2; and the solid electrolyte, which moves the ions that build up in the cathode to the anode. The solid electrolyte's ion conductivity efficiency is crucial in achieving high electrical efficiency between all the parts involved in the fuel cell. Owing to the potential for thermal and structural stability when subjected to elevated operating temperatures exceeding 800 °C. Yttrium-doped zirconia-based electrolytes are one of the first solid oxide ceramic electrolytes developed for this purpose, gaining importance from many researchers [2, 3]. The ceramic electrolytes composed of Yttria-stabilized zirconia (YSZ) exhibit a notable ionic conductivity of approximately 0.1 $(\Omega\ cm)^{-1}$ within the temperature range of 800–1000 °C. Nonetheless, SOFCs have encountered several challenges with high operating temperatures, including material corrosion within cell parts. Consequently, SOFCs are compelled to operate at intermediate (500–700 °C) and low (500 °C) temperatures [4–6]. The δ-Bi_2O_3 material exhibits significant oxygen-ion conductivity, making it an appropriate candidate for employment as a solid electrolyte in low-temperature SOFC technology.

Regardless of the extensive studies conducted in this field, the full capabilities of δ-Bi_2O_3 have not been adequately explored, considering its total conductivity of approximately 3 $(\Omega\ cm)^{-1}$ at 800 °C [7, 8]. Due to the inherent characteristic of this high-temperature polymorph, it exhibits stability solely within a narrow temperature range, specifically between 730 and 825 °C [6]. Consequently, its applicability in intermediate-temperature SOFCs is restricted. In a more precise manner, it can be observed that the α-Bi_2O_3 polymorph, which exhibits stability at low temperatures, undergoes a phase transition to the δ-Bi_2O_3 phase at a temperature of 730 °C. Subsequently, the δ-Bi_2O_3 phase undergoes melting when further heated to approximately 825 °C [8]. However, several studies have shown that doping with rare-earth elements can stabilize the δ-Bi_2O_3 polymorph [9–13]. The ionic radius of dopant has been emphasized in the literature, as it plays a major role in stabilizing the cubic δ-phase and attaining elevated levels of electrical conductivity. Several stabilization investigations have demonstrated that utilizing small radii dopants in the Bi^{3+} site can aid in stabilizing the δ-phase. Conversely, using greater lanthanides like La results in a distorted structure symmetry with lower ionic conductivity than the stabilized δ-Bi_2O_3, as reported in studies [14, 12, 15–17]. In contrast, the polarizability of cations, which exhibits a direct relationship with the cubic value of cation radii, plays a critical role in attaining optimal conductivity levels within doped Bi_2O_3 ceramics. The Bi^{3+} cation exhibits a notable polarization capacity in contrast to the lanthanide group elements [1, 17], owing to the presence of its 6 s_2 single pair electrons. The partially substituting cations between the host Bi^{3+} and dopants decrease polarizability, notably impacting electrical conductivity. In the current study, we are striving to achieve a higher level of oxygen ion conductivity than what has been reported in previous literature. To accomplish this, we are exploring the use of mixed-valence cation doping, such as rare earths, in the crystal lattice of Bi_2O_3. This approach could promote the formation of oxygen vacancies while stabilizing the δ-phase ceramics and achieving

a superior conductivity at a lower operating temperature than reported in the previous work. The highest conductivity, with lowered impedance ceramic could serve as a promising candidate for application as a solid electrolyte in Solid Oxide Fuel Cell (SOFC) devices. Hence, despite stabilizing the δ-polymorphic phase, a significant concentration of dopants reduces electrical conductivity due to the diminished polarization capability [18, 19]. The concept of polarization power in ceramic systems refers to the capacity of a cation to perturb the electron cloud of an anion in the sublattice or to attract the electron density of an anion itself [18–22]. To attain elevated oxygen ion conductivity, it is imperative to select the dopant that stabilizes the cubic δ-phase meticulously. Some reports demonstrated that bi-doping methods are more effective than single-doping processes in enhancing conductivity and facilitating stabilization in doped δ-Bi_2O_3 systems [23, 24]. The study by D.W. Jung et al. explored the bi-doping approach utilizing tungsten and dysprosium cations, known for their strong polarizability. It achieved the maximum electrical conductivity of 0.570 $(\Omega\ cm)^{-1}$ at 700 °C and 0.098 $(\Omega\ cm)^{-1}$ at 500 °C. They consistently emphasized that to get the maximum conductivity, the total amount of dopant and the additive material ratio must be maintained at 12% and 2:1, respectively [23, 24]. The scientific investigation of binary system electrolytes has revealed that most of them exhibit the stable cubic δ-Bi_2O_3 phase, and their conductivities range from approximately 10^{-7} to 10^{-2} $(\Omega\ cm)^{-1}$, as reported in the literature [25, 26]. According to Punia et al.'s findings, incorporating Bi_2O_3 into zinc vanadate results in a structural transformation from VO_4 tetrahedral to VO_5 trigonal bipyramid, leading to a notable increase in density and molar amount [27]. Furthermore, materials doped with alkaline ions typically exhibit electronic and ionic conductivity phenomena that vary with temperature changes. Bismuth vanadate that has been doped exhibits a notable electrical conductivity of approximately 0.2 $(\Omega\ cm)^{-1}$ at a temperature of 500 °C. This is attributed to the increased presence of oxygen vacancies and the stabilization of the highly conductive γ-phase at room temperature, as previously reported [28]. M.Kış et al. presented an investigation into the electrical properties of Dy-Sm double-doped Bi_2O_3-based materials. These materials are considered potential candidates for SOFC electrolytes [29]. The research examined structural and temperature effects on these materials' electrical characteristics. The stable δ-phase compounds had higher conductivities. They demonstrated that $Bi_{0.6}Dy_{0.2}Sm_{0.2}O_{1.5}$ exhibited the highest electrical conductivity of 2.5×10^{-2} $(\Omega\ cm)^{-1}$ at a temperature of 750 °C. Moreover, Y. Polat et al. investigated the ternary system of $Bi_{1-x-y}Sm_xYb_yO_{1.5}$, which was prepared through a solid-state reaction. They found that $Bi_{0.8}Sm_{0.1}Yb_{0.1}O_{1.5}$ nanostructured ceramics had the highest electrical conductivity of 5.39×10^{-2} $(\Omega\ cm)^{-1}$ at 650 °C. This nanostructure is the most suitable dopant concentration. This is primarily attributed to its favorable stability and oxygen ionic conductivity, both critical factors in the design of the electrolyte layer in SOFCs [30]. One of the major benefits of double doping is that it helps to maintain phase stability using a low doping rate, as opposed to the larger doping rate required in single doping [12, 14]. As a result, co-doping has shown that the optimal doping level needed for phase stability can potentially be reduced when compared to single doping [26]. In the current study, we are striving to achieve a higher level of oxygen ion conductivity than what has been reported in previous literature by using the double-doping approach. To accomplish this, we are exploring the use of mixed-valence cation doping, such as rare earths, in the crystal lattice of Bi_2O_3. This approach could promote the formation of oxygen vacancies while stabilizing the δ-phase ceramics and achieving a superior conductivity at a lower operating temperature than reported in the previous work. The highest conductivity, with lowered impedance ceramic, could serve as a promising candidate for application as a solid electrolyte in Solid Oxide Fuel Cell (SOFC) devices. This advancement could potentially offer higher efficiency and improved performance of the fuel cell technology.

To the best of our knowledge, no previous study has been performed on $Bi_{1-x-y}V_xDy_yO_{1.5}$ ternary ceramic systems with varying values of x and y ($y = 0.05/x = 0.05$, 0.10, 0.15, and 0.20, and $x = 0.05/y = 0.10$, 0.15, and 0.20). In the present study, we stabilized the cubic fluorite type δ-Bi_2O_3 and improved its conductivity through doping with rare earth (Dy_2O_3) and transition metal (V_2O_5) oxides. We thoroughly analyzed the effects of varying mixed valence cations and dopant content ratios on the structure, phase stability, morphology, electrical conductivity, and electrochemical performance using a double-doping approach, ensuring a low mutual doping ratio. Vanadium oxide (V_2O_5) is an appealing choice for implementing SOFCs operating at lower temperatures (600–800 °C) due to its excellent

conductivity at such temperatures. The electrical conduction in V_2O_5 ceramics happens due to the exchange of unpaired 3d1 electrons between the valence states of V^{4+} and V^{5+}. This exchange happens in a pattern of V^{4+}–O^{2-}–V^{5+}–O^{2-}–V^{4+}, inducing polarization and forming polarons [31]. All compositions were synthesized through solid-state reactions under atmospheric conditions. The structural and microstructural investigations of the synthesized compositions were performed through X-ray diffraction (XRD) and X-ray photoelectron spectroscopy (XPS). The thermal properties and possible phase transitions were characterized using the Thermo-gravimetric and Differential Thermal Analysis (DTA/TGA). The programmable Four-Point Probe Technique (FPPT) was employed to perform conductivity tests under an air atmosphere. Based on the electrochemical impedance spectroscopy (EIS), the electrochemical performance of the designed cells was evaluated. Finally, the surface morphology of the as-sintered pellets was performed by Field Emission–Scanning Electron Microscope (FESEM).

2 Experimental details

2.1 Experimental procedures

The high-purity oxide powders of Bi_2O_3, V_2O_5, and Dy_2O_3 (99.99% purity, Sigma Aldrich) were utilized to synthesize the ternary systems of $Bi_{1-x-y}V_xDy_yO_{1.5}$ ($y = 0.05/x = 0.05$, 0.10, 0.15, and 0.20, and $x = 0.05/y = 0.10$, 0.15, and 0.20). The ceramic series was synthesized using the solid-state route, ensuring their high quality. The mutual doping ratios of the fabricated ceramics are precisely presented in Table S1 (supporting material) for reference. The raw precursor materials were vigorously mixed in ethanol for 2 h. The stoichiometric powders were ground in an agate mortar for 20 min to ensure optimal quality. Once all the powder mixtures were prepared, they were efficiently divided into two sections. One section was carefully packed into alumina boats, while another was meticulously pressed into pellets. Both sections were then expertly subjected to thermal processing inside a controlled muffle furnace at a temperature of 800 °C for 100 h. This ensured that the powder mixtures were optimally treated for their intended purpose. During the calcination process, the materials were heated assertively at a steady rate of 5 °C/min in open-air conditions. Heat treatment was conducted on all compositions to meet several objectives, such as enhancing the quality of densification, eliminating unwanted impurities, and ensuring phase stability. A portion of the powders was subsequently utilized to fabricate pellets with a diameter of 13 mm and a thickness of 0.51 mm, using a Specac Ltd. manual pressing machine with a mechanical pressure of 10 tons.

2.2 Characterization techniques

The PANalytical X'Pert pro MRD diffractometer was used to investigate the structural characteristics of the synthesized compositions. The tool utilizes Cu-Kα ($\lambda = 1.54056$ Å) radiation operated at 45 kV and 40 mA over the range 10–90° (2θ), with a scanning rate of 0.01°/sec per step. The Panalytical Highscore Plus and FullProf Suite programs were used to analyze the XRD patterns of the pure δ-phase $Bi_{1-x-y}V_xDy_yO_{1.5}$ ternary system and identify their crystallite parameters such as crystallite size and lattice strain. Fullprof software allowed for precisely determining various structural parameters, including lattice dimensions and integrated breadth. The structural refinement for pure δ-phase ceramics was initiated using powder diffraction data [32]. For deep structural analysis of the prepared ceramics, X-ray photoelectron spectroscopy (XPS) spectra were gathered using precise monochromatic X-ray Al K-alpha irradiation featuring a 400 µm spot size, 10^{-9} mbar pressure, and a complete spectrum sweep energy of 200 eV on K-ALPHA, supplied only by the world-renowned Thermo Fisher Scientific, USA. The collected core-shell spectra were deconvoluted after removing the Shirely background. The thermal characteristics of the ceramics were precisely determined through thermogravimetry/differential thermal analysis (TG/DTA) measurements. The tests were carried out using a Perkin Elmer-Diamond analyzer with a constant heating rate of 5 °C/min. The temperature was raised until it reached approximately 800 °C from the initial room temperature. The DTA curves were meticulously checked to ascertain the occurrence of a phase transition during consistent heating. The TG curves were analyzed concerning temperature to determine potential mass changes resulting from chemical reactions, such as oxidation, that may occur during heating. The pellets' morphological characteristics were thoroughly analyzed utilizing Quanta FEG-250 FESEM equipment. The samples were coated with a layer of gold to achieve

higher-resolution images using a sputtering technique. The Four Point Probe Technique (FPPT) was employed to measure the conductivities of such pellets with exceptional precision across an extensive temperature range of 30 to 800 °C. We employed the highly reliable and precise Keithley 2400 and 2700 tools to ensure the highest possible accuracy. High-purity platinum cables, with a diameter of 0.5 mm, were firmly positioned at identical distances on the pellet surface, ensuring zero contact resistance. These wires were utilized as current and voltage channels during the measurement process. The temperature was determined accurately using K-type thermocouples, which were positioned in close proximity to the pelletized samples. The impedance of the samples was measured using the highly reliable EIS technique. The measurements were taken with the highest precision and accuracy using (Ivium Vertex. One EIS–Potentiostat). The data was collected with a potential range of ± 10 V with a resolution of 0.08 mV and a current range of 100 pA–100 mA across a frequency range from 1 Hz to 100 kHz. The obtained data was analyzed using the IviumSoft ^{TM} data processing program to ensure thorough scrutiny and interpretation of the results.

3 Results and discussion

3.1 Structural characteristics of the ternary system

The XRD data of synthesized ceramics labeled M1–M7 were analyzed before and after electrical measurements at 750 and 800 °C, respectively. Figure 1a,b displays the X-ray diffractograms for both calcination stages. These diffractograms are indicative of the structural characteristics of the samples. The XRD analysis unambiguously confirmed the existence of both α- and δ-phases in the pre-calcinated powder (M3–M7), while the patterns obtained for samples M1 and M2, strongly indicated the existence of a δ-Bi_2O_3, as depicted in Fig. 1a. It is evident from Fig. 1b that the final calcination step led to the formation of the δ-phase polymorphs.

The Rietveld refinement method is based on fitting a model diffraction pattern to the step-scan data of the entire XRD patterns of pure δ-phase ceramics, utilizing a weighted least-squares approach. This process identifies peaks at specific angles, $2\theta = 28.2^o$, 32.7^o, 46.9^o, 55.7^o, 58.4^o, 68.5^o, 75.7^o, 78.0^o, and 86.34^o. These peaks correspond to specific crystallographic planes (111), (200), (202), (311), (222), (331), (420), and (422), respectively. The diffraction pattern obtained closely matched

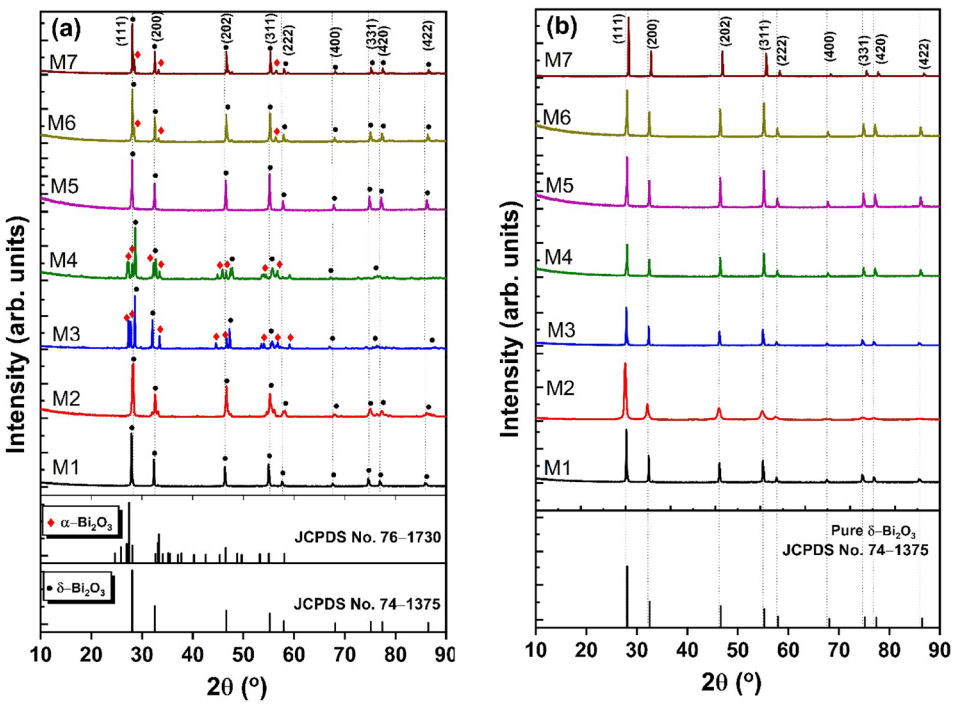

Fig. 1 XRD patterns of the synthesized compositions, definitely **a** before conductivity measurements at 750 °C, and **b** after conductivity measurements at 800 °C

the standard card (JCPDS No. 74–1375) associated with the Fm-3m (No. 225) space group. This particular space group exhibits six oxygen atoms at the 8-fold positions (8c site) [33]. It has been observed through Rietveld refinement analysis that the selected sample $Bi_{0.90}V_{0.05}Dy_{0.05}O_{1.5}$ has stabilized the δ-phase without any foreign peaks from any impure phases. This is evident in Fig. 2. Moreover, the profile fitting of the other ceramics, as illustrated in Fig. S1a–f, also confirms the presence of stabilized fcc δ-phase samples. Based on the noticed sharp-intensity signals, it is evident that the prepared materials possess a high level of crystallinity. Willis' theoretical scenario, which postulates the existence of six O atoms randomly distributed via (111) orientations, stretching from tetrahedral positions to the core octahedral site (32f), lends more credence to this finding [34, 35]. *Boyapati et al.* conducted a study revealing that oxygen atoms transition from the 8-fold positions (8c) to 32f octahedral positions [36]. Similarly, Battle et al. found that the anion sublattice combines Gattow and Willis models, where oxygen anions are located at 8c and 32f locations. It is important to note that the empty oxygen sites unequivocally exhibit a strong preference for encircling the Bi atoms in the (111) direction. The results were crucial in analyzing the structure of δ-phase ceramics, confirmed by accurately matching the XRD data profiles. The three-dimensional electron density visualization map of the stabilized $Bi_{0.90}V_{0.05}Dy_{0.05}O_{1.5}$ confirms the observations, as demonstrated in Fig. S2 (supporting material). The methods described employ the robust Fourier and highly efficient fast Fourier transform (FFT) methodology. The 3-D visualization clearly illustrates that the black boundary line unambiguously represents heightened electron density levels surrounding Bi (III) ions. The colored regions, on the other hand, showcase varying shades from green to violet-brown, indicating significant discrepancies between the two. Substantial displacements of O atoms in the unit cells can be observed, which are in stark contrast to the positions of Bi. The peaks associated with the locations of (4a) show significant prominence, while those related to oxygen positions at tetrahedral and octahedral sites are minuscule. The findings presented in Fig. S2 provide further elaboration on this information. The full detailed crystallite and fitting parameters of the fcc δ-phase ceramics are precisely outlined in Table 1, based on the Rietveld profile results. As displayed in Figs. 2 and S1, the refinement profile fitting exhibits exceptional fitting, as evidenced by the χ^2 values being less than 2. This robust goodness of fit is a strong testament to the accuracy of the results.

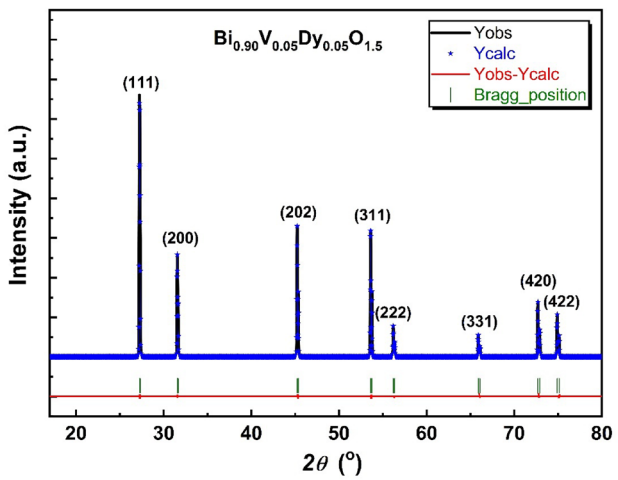

Fig. 2 Rietveld refinement of XRD data of cubic stabilized $Bi_{0.90}V_{0.05}Dy_{0.05}O_{1.5}$. The vertical green line shows the estimated Bragg reflection points. The lower red line represents the difference between the observed and calculated patterns

The mean crystallite sizes (D) were determined using the Scherrer-Warren Equation

$$D = k\lambda/\left(\beta_{hkl}\cos\theta\right) \tag{1}$$

Table 1 showcases the XRD findings that indicate a considerable reduction in D values. The greater dislocation density and point defect generation observed may be attributed to substituting Bi^{3+} cations with dopant cations such as Dy^{3+} and V^{5+}. This substitution results in an increased number of vacant anion positions inside the crystal structure, possibly generating an electrically induced anion sublattice. As for rare-earth doping, it's worth noting that the anion removal process from the lattice may induce lattice strain, thus contributing to the observed decrease in average crystallite size, as exemplified by the data in Table 1 [37]. In addition to determining the crystal structure of the δ-phase ceramics, the current study also calculated other important structural features, such as dislocation density (δ), stacking fault (SF), and lattice strain (ε) [33]. Table 1 lists the values of these parameters, which are calculated using Eqs. (2, 3, 4).

$$\delta = \frac{1}{D^2} \tag{2}$$

Table 1 Refined crystallite parameters and fitting parameters of all the cubic δ-phase stabilized compositions achieved by the Rietveld analysis in space group 'Fm-3m'

Sample code	Composition	Unit cell parameters		Crystallite parameters			Lattice Strain (ε)	Fitting parameters				
		a (Å)	V (Å^3)	Mutual dopant ratios	Average crystallite size (nm)	Dislocation density δ (10^{-4}nm^{-2})		Stacking Fault ($SF\times10^{-2}$)	R_{WP} (%)	R_{exp} (%)	RB (%)	RF (%)	χ^2
M1	$Bi_{0.90}V_{0.05}Dy_{0.05}O_{1.5}$	5.53045	169.154	1:1	46.5 ± 3.40	4.62	0.021	2.21	55.30	50.23	2.10	2.39	1.21
M2	$Bi_{0.85}V_{0.10}Dy_{0.05}O_{1.5}$	5.52232	168.408	2:1	44.4 ± 3.33	5.07	0.023	2.53	57.60	53.23	2.34	2.66	1.17
M3	$Bi_{0.80}V_{0.15}Dy_{0.05}O_{1.5}$	5.51745	167.964	3:1	32.1 ± 2.41	9.70	0.053	3.51	57.20	50.43	2.12	2.43	1.28
M4	$Bi_{0.75}V_{0.20}Dy_{0.05}O_{1.5}$	5.59123	174.792	4:1	30.6 ± 3.40	10.67	0.056	4.63	55.23	48.14	2.71	2.40	1.31
M5	$Bi_{0.85}V_{0.05}Dy_{0.10}O_{1.5}$	5.58245	173.970	1:2	62.2 ± 4.66	2.58	0.031	3.84	55.13	49.16	2.14	2.37	1.12
M6	$Bi_{0.80}V_{0.05}Dy_{0.15}O_{1.5}$	5.53812	169.858	1:3	47.1 ± 2.99	4.50	0.022	4.47	55.60	50.52	2.46	2.61	1.21
M7	$Bi_{0.75}V_{0.05}Dy_{0.20}O_{1.5}$	5.49921	166.303	1:4	40.1 ± 3.67	6.21	0.025	3.43	57.21	51.43	2.56	2.51	1.11

$$\varepsilon = \frac{\beta_{hkl}}{4\ \tan\theta} \tag{3}$$

$$SF = [\frac{[2\pi^2]}{45\ \sqrt{\tan\theta}} \cdot \beta \tag{4}$$

Intrinsic stacking faults (SFs) are known to originate from the accumulation of vacancies or aggregation of interstitials. The microstructures synthesized in the current study exhibit an impeccable arrangement of lattice planes and a notable absence of significant defects. Table 1 shows a direct correlation between the decrease in crystallite size and increased lattice stain, as predicted by Eq. (2) [33]. Table 1 illustrates that the lattice parameters obtained from the cubic δ-phase compositions are lower than those of pure δ-Bi_2O_3 (5.6595 Å). This reduction in the lattice constant is attributed to utilizing relatively more minor cations than the host Bi^{3+} cation. The exchange of cations between rare-earth cations and host Bi^{3+} ions results in lattice reduction. The ionic radii of Bi^{3+}, Dy^{3+}, and V^{5+} in octahedral locations have a significant impact on this phenomenon. According to L. Gui et al. [38], the ionic radii of Bi^{3+}, Dy^{3+}, and V^{5+} are 1.03, 0.912, and 0.54 Å, respectively. Furthermore, Table 1 clearly shows that increasing the overall dopant concentration in the composition leads to a reduction in crystallite size. This effect can be attributed to an elevation in the lattice strain (ε) resulting from a significant enhancement in dislocation densities, indicating crystal imperfections such as dislocation. Loading V^{5+} and Dy^{3+} into the pristine Bismuth (III) oxide causes a size reduction, accompanied by the natural formation of non-uniform crystal defects primarily associated with lattice strain [39, 40].

For deep insight into the structure, composition, and bonding states of the $Bi_{1-x-y}V_xDy_yO_{1.5}$ ceramic systems, X-ray photoelectron spectroscopy (XPS) was performed. The full-range XPS survey scan of a $Bi_{0.85}V_{0.10}Dy_{0.05}O_{1.5}$ is shown in Fig. 3a, demonstrating the presence of bismuth (Bi 4f), dysprosium (Dy 3d), vanadium (V 2p), carbon (C 1s), and oxygen (O 1s) in the ceramic material. Figure 3a displays the XPS survey scan of a ceramic material with the chemical composition $Bi_{0.85}V_{0.10}Dy_{0.05}O_{1.5}$. The scan indicates the presence of several elements, including bismuth (Bi 4f), dysprosium (Dy 3d), vanadium (V 2p), carbon (C 1s), and oxygen (O 1s). According to the data provided, the contents of Bi, Dy, V, C,

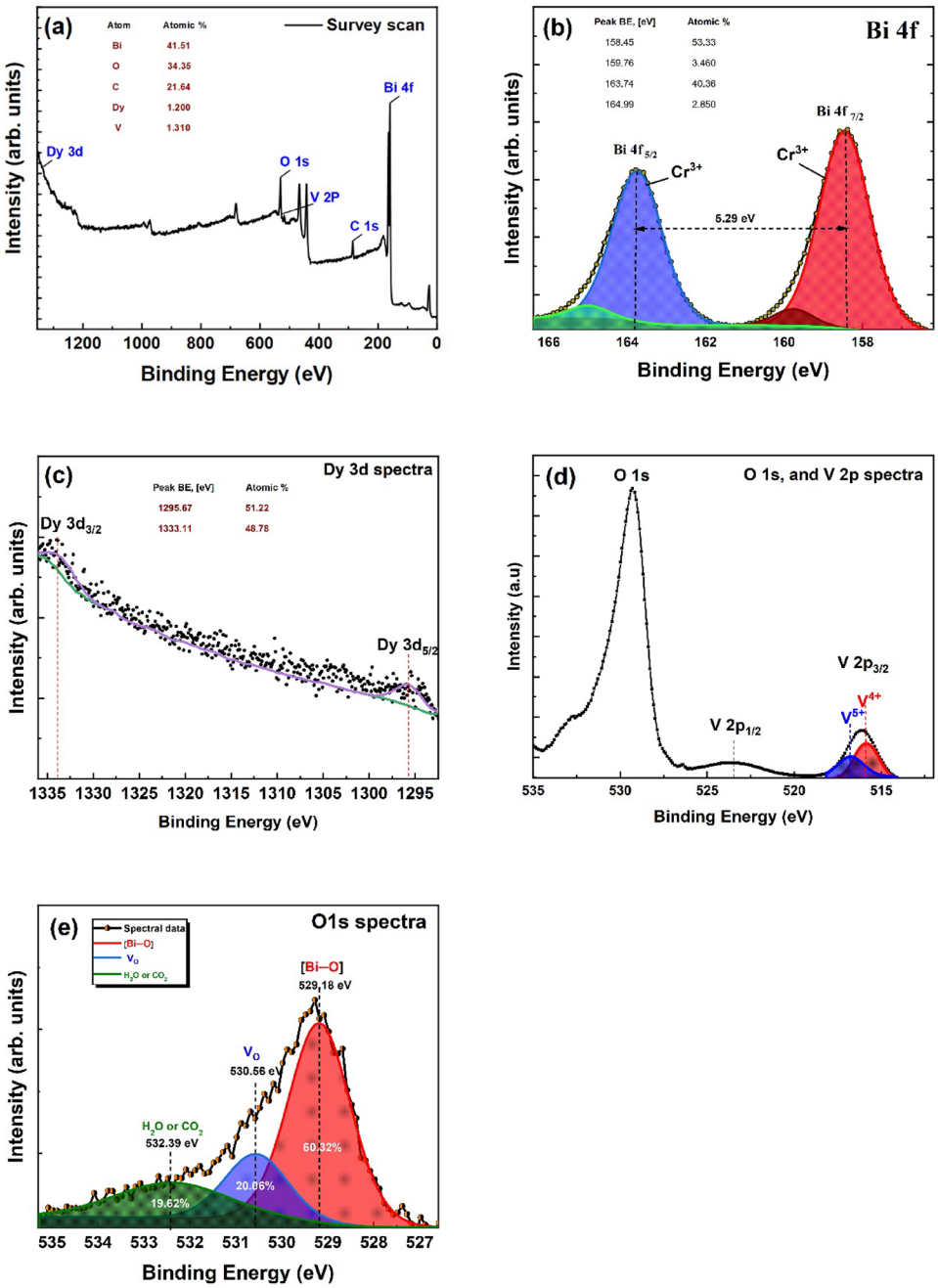

Fig. 3 **a** XPS survey spectra of $Bi_{0.85}V_{0.10}Dy_{0.05}O_{1.5}$ composition. High-resolution deconvoluted core level spectra of **b** Bi 4f, **c** Dy 3d, **d** V 2p, and **e** O 1s

and O elements in the $Bi_{0.85}V_{0.10}Dy_{0.05}O_{1.5}$ pellet were calculated to be 21.64, 1.20, 1.31, 41.51, and 34.35%, respectively. The XPS full scan shows a carbon C 1s peak at a binding energy of 285 eV, attributed to contamination from atmospheric sources and adventitious carbon from the XPS instrument. In fact, a significant concentration of carbon contamination is typically observed in most samples exposed to the atmosphere.

The Bi 4f spectra in Fig. 3b reveal two distinct peaks at binding energies (BE) of 163.74 and 158.45 eV, corresponding to Bi $4f_{7/2}$ and Bi $4f_{5/2}$ spin orbits, respectively [41]. The spin-orbit separation between these peaks is 5.29 eV. As per the available literature, no significant shift is observed in the binding energy values of the peaks. This observation strongly suggests the existence of bismuth in the Bi^{+3} state. The presence of two less prominent peaks at higher binding energy 159.7 eV

(Bi $4f_{7/2}$) and 165.0 eV (Bi $4f_{5/2}$) among the four deconvoluted peaks can be attributed to a surface charging effect caused by a change in the polarization of the $Bi_{0.85}V_{0.10}Dy_{0.05}O_{1.5}$ crystal and suggesting the existing of Bi^{3+} [42]. Furthermore, the Dy 3d spectra illustrated in Fig. 3c reveal two peaks associated with the spin-orbit splitting of Dy $3d_{5/2}$ and Dy $3d_{3/2}$ at binding energies of 1295.67 and 1333.11 eV, respectively [43]. As per the methodology in [44], O1s and V2p XPS photolines were analyzed. According to reports, the O1s region with binding energy (BE) of 530 eV falls within the range used to determine the Shirley background underlying the V2p zone. The O1s core level with a binding energy of 530.0 eV is an absolute internal reference for BE. The binding energy of the $V2p_{3/2}$ core level remains constant for all oxidation states of vanadium in proportion to the O1s level. Additionally, the signal portions of $V2p_{3/2}$ and $V2p_{1/2}$ are rigidly limited to a 3:1 ratio. It is worth mentioning that vanadium can be present in ceramics in two oxidation states, V^{4+} and V^{5+}. In a previous study, VOx-grafted TiO_2 nanoparticles were used as an efficient anode catalyst, and it was observed that V^{5+} has a $2p_{3/2}$ binding energy (BE) of approximately 517.3 eV, while V^{4+} is at a BE of around 516.1 eV [45]. In the V 2p spectra, there are two distinguishable peaks. The first peak is specifically for V $2p_{3/2}$, and the other peak, confidently attributed to the V $2P_{1/2}$ spin state, is observed at 523 eV. Therefore, the V $2p_{3/2}$ core level peak may be divided into two components: one originating from V^{4+} ions with a BE of ~ 516 eV and the other from V^{5+} ions with a BE of 517.2 eV, as shown in Fig. 3d. The deconvolution of the $V2P_{3/2}$ peak shows that both V^{4+} $2p_{3/2}$ and $V^{5+}2p_{3/2}$ are present in signal areas with a ratio of approximately 2:1 [45]. The O 1s deconvoluted spectra of the sample under investigation are presented in Fig. 3e. The analysis of the spectra exhibits three distinct peaks with utmost clarity. The first peak at a binding energy (BE) of 529.18 eV is attributed to Bi^{3+}–O^{2-} [46]. The second component, between 530.5 ± 0.5 eV, is attributed to the O^{2-} in the oxygen-deficient (V_O) region within the matrix of $Bi_{0.85}V_{0.10}Dy_{0.05}O_{1.5}$ [46]. The third peak identified at a BE of 532.39 ± 1 eV is unequivocally associated with adsorbed oxygen species, specifically H_2O and CO_2 [47].

3.2 TG/DTA thermal analysis

The thermal characteristics of the compositions, as observed through the TG/DTA system, are depicted in Fig. 4. In Fig. 4a, the TG results (represented by the red and green line) demonstrate the weight loss experienced by samples M4 ($Bi_{0.75}V_{0.20}Dy_{0.05}O_{1.5}$) and M7 ($Bi_{0.75}V_{0.05}Dy_{0.20}O_{1.5}$) throughout thermal treatment. The TG curve reveals that the heating process does not result in any significant mass loss, which shows that the chart experiences minimal fluctuations of only 0.1%, indicating that the compositions can maintain stability even under high-temperature conditions. The other synthesized ceramics also exhibited the same observation, as demonstrated by the TG curves in Fig. S3 (Supplementary material). Under similar conditions encountered through electrical investigations, it may be argued that higher-temperature regions show a significant thermal and structural stability level. Furthermore, the increase in oxygen voids (Vo)

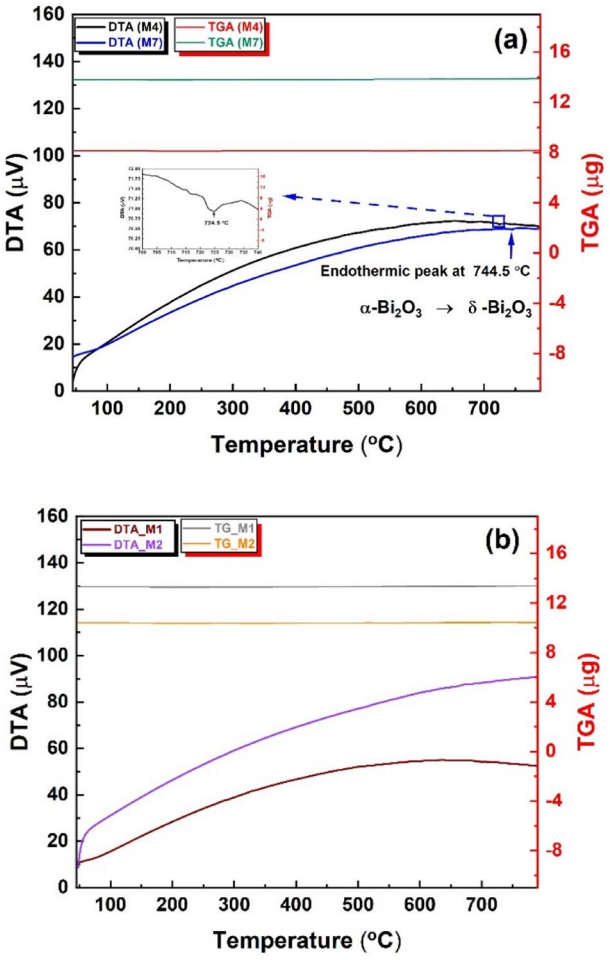

Fig. 4 TG-DTA curves of **a** two different samples, $Bi_{0.75}V_{0.20}Dy_{0.05}O_{1.5}$ and $Bi_{0.75}V_{0.05}Dy_{0.20}O_{1.5}$, during the order-disorder transition, and **b** FCC stabilized samples $Bi_{0.90}V_{0.05}Dy_{0.05}O_{1.5}$ and $Bi_{0.85}V_{0.10}Dy_{0.05}O_{1.5}$

in the sublattice resulting from the doping process indicates that removing O^{2-} ions from the sublattice and their conversion into oxygen gases may be a possible explanation for the temperature-dependent weight loss [33]. The DTA analysis clearly indicates the presence of a broad endothermic peak in the range of 700 to 745 °C through the heating process of samples M4 and M7 (black and blue lines), as depicted in Fig. 4a. The selected samples showed an endothermic peak during the heating process, as indicated by DTA. For $Bi_{0.75}V_{0.20}Dy_{0.05}O_{1.5}$, the process started at T_{onset}= 720 °C and ended at T_{end}= 728 °C. Similarly, for $Bi_{0.75}V_{0.05}Dy_{0.20}O_{1.5}$, the process started at T_{onset}= 744.4 °C and ended at T_{end}= 744.6 °C. The loading of V^{5+} and Dy^{3+} in the ternary ceramic system results in a slight shift in T_{onset} between samples M4 and M7. The endothermic peak in the DTA curves is caused by the order-disorder transition (ODT) [33]. This observation is consistent with the XRD data (Fig. 1a) that indicates the presence of the δ-phase and a small percentage of the α-phase in the samples under investigation. Additionally, the DTA curves for Samples M1 ($Bi_{0.90}V_{0.05}Dy_{0.05}O_{1.5}$) and M2 ($Bi_{0.85}V_{0.10}Dy_{0.05}O_{1.5}$) demonstrate thermal stability up to 800 °C without any observable endothermic peaks. This lack of an endothermic peak in M1 and M2, as illustrated in Fig. 4b, agrees with the XRD findings (Fig. 1a). The ODT is contingent upon the occupation of a sublattice within the distorted defect crystal structure of the fcc δ-phase Bi_2O_3, characterized by oxygen ion vacancies. The XPS results corroborate this observation. The oxygen lattice points of the δ-phase Bi_2O_3, doped with V and Dy, are observed to be partially occupied by oxygen ions. During solid-state processing involving loading of V_2O_5 and Dy_2O_3 in the δ-Bi_2O_3 crystal lattice, it has been noted that the cations of V^{5+} and Dy^{3+} exhibit a preference for substitution at the face-centered cubic (fcc) sites within the crystal structure. The evidence strongly suggests that Dy_2O_3 and V_2O_5 can dissolve in the δ-Bi_2O_3 matrix. Furthermore, certain oxygen lattice points placed near the fcc sites will likely remain vacant, ultimately creating an anion vacancy in the structure.

The FCC crystal structure demonstrates the fluorite structure with a deficiency of oxygen, having two units per cell and two empty locations for oxygen ions in each unit cell. The bismuth ions are positioned on the FCC sites inside the structure, differing solely in their arrangement relative to the oxygen ions [48]. The observed scenario in conductivity measurements consistently indicates a transition from the low-temperature range (LTR) to the high-temperature range (HTR), which can be attributed to the onset of the ODT. Furthermore, the high-temperature regions exhibit remarkable thermal and structural stability. The endothermic reaction and electrical conductivity transition suggest the exact transport mechanism due to differences in the occupancy of oxide ion locations (8c and 32f) [33].

Fig. 5 FESEM micrographs showing the pores architecture and interconnectivity for the as-sintered pellets **a** $Bi_{0.90}V_{0.05}Dy_{0.05}O_{1.5}$, **b** $Bi_{0.85}V_{0.10}Dy_{0.05}O_{1.5}$, **c** $Bi_{0.80}V_{0.15}Dy_{0.05}O_{1.5}$, **d** $Bi_{0.75}V_{0.20}Dy_{0.05}O_{1.5}$, **e** $Bi_{0.85}V_{0.05}Dy_{0.10}O_{1.5}$, **f** $Bi_{0.80}V_{0.05}Dy_{0.15}O_{1.5}$, **g** $Bi_{0.75}V_{0.05}Dy_{0.20}O_{1.5}$, and **h** The apparent porosities of samples as a function of Dy content

3.3 The morphological characteristics of the sintered pellets

After conducting conductivity measurements, a field-emission scanning electron microscope (FESEM) was used to thoroughly analyze the surface morphologies of the prepared pellets at ambient temperature. Figure 5 demonstrates the FESEM morphology of the surfaces and fractures of all the prepared pellets. The micrographs consistently showed the presence of non-uniform and aggregated grains. The degree of aggregation was observed to be more prominent as the concentration of Dy^{3+} loading increased, in contrast to the 5–20 wt% vanadium loading, as illustrated in Fig. 5. The estimated mean grain size of the as-sintered pellets varies from 0.80 to 5.57 µm. The FESEM images demonstrate that neither $Bi_{0.90}V_{0.05}Dy_{0.05}O_{1.5}$ nor $Bi_{0.85}V_{0.10}Dy_{0.05}O_{1.5}$ samples exhibit any visible pore formation, even under higher magnification, as shown in Fig. 5a, b. The microstructure of Dy-5wt% pellets sintered at 800 °C, significantly improving its density. The sintering process led to well-defined grain boundaries and a complete absence of porosity, as evidenced by Fig. 5a, b. Conversely, the corresponding data in Fig. 5e–g reveal a noticeable increase in pore formation with an increase in Dy^{3+} content. The presence of voids depicted in Fig. 5e–g that display irregular diameters indicates the porous nature of ceramics, consistent with previous studies' findings as reported in the literature [33, 49]. Remarkably, the texture control of a material has a considerable influence on its

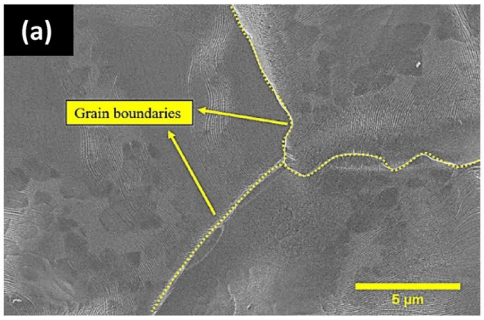
(a)
Grain boundaries
5 µm

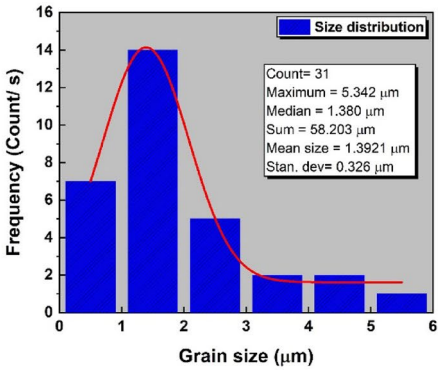
Size distribution
Count= 31
Maximum = 5.342 µm
Median = 1.380 µm
Sum = 58.203 µm
Mean size = 1.3921 µm
Stan. dev= 0.326 µm
Frequency (Count/ s)
Grain size (µm)

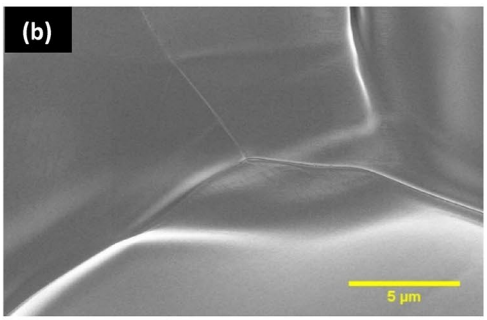
(b)
5 µm

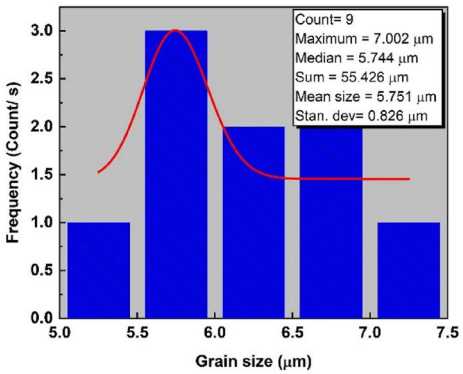
Count= 9
Maximum = 7.002 µm
Median = 5.744 µm
Sum = 55.426 µm
Mean size = 5.751 µm
Stan. dev= 0.826 µm
Frequency (Count/ s)
Grain size (µm)

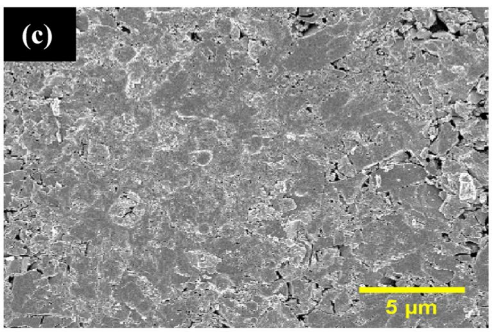
(c)
5 µm

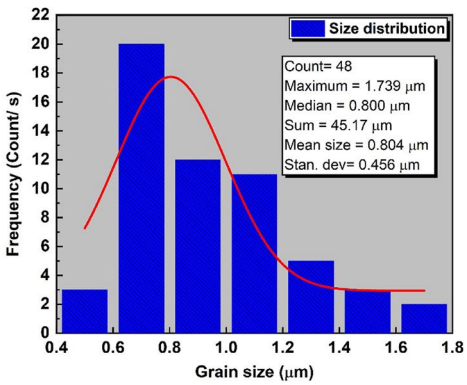
Size distribution
Count= 48
Maximum = 1.739 µm
Median = 0.800 µm
Sum = 45.17 µm
Mean size = 0.804 µm
Stan. dev= 0.456 µm
Frequency (Count/ s)
Grain size (µm)

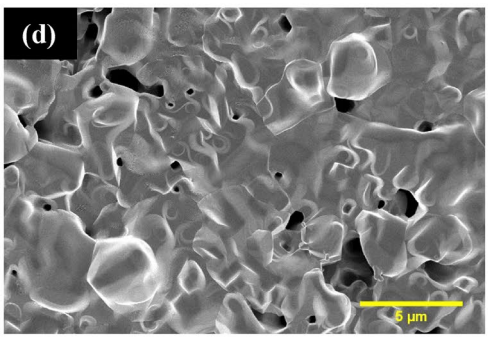
(d)
5 µm

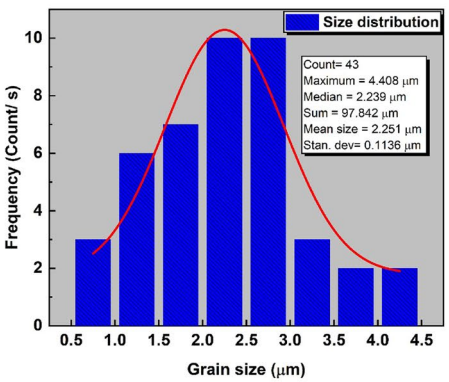
Size distribution
Count= 43
Maximum = 4.408 µm
Median = 2.239 µm
Sum = 97.842 µm
Mean size = 2.251 µm
Stan. dev= 0.1136 µm
Frequency (Count/ s)
Grain size (µm)

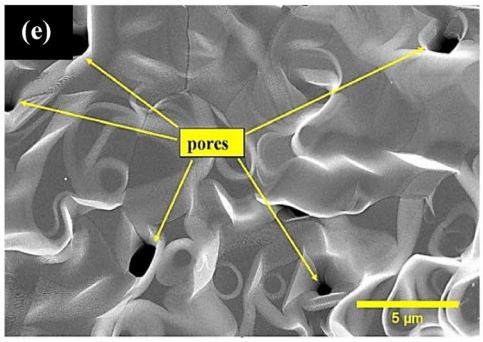

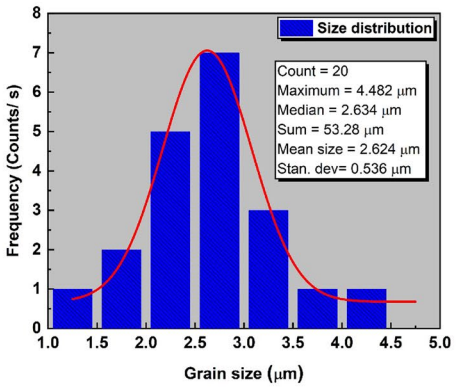

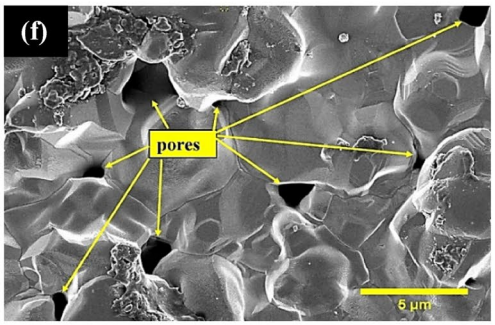

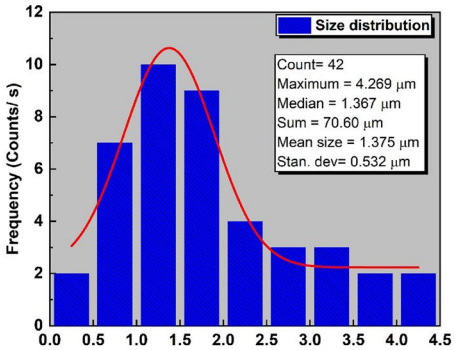

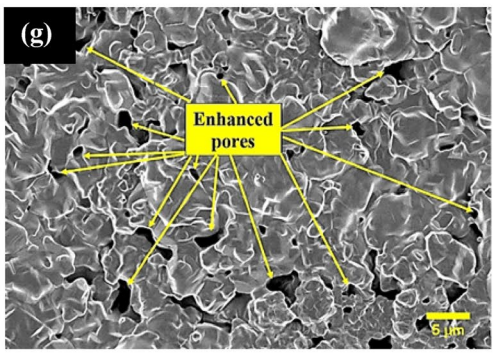

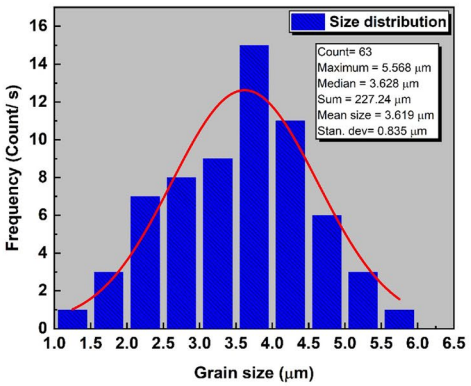

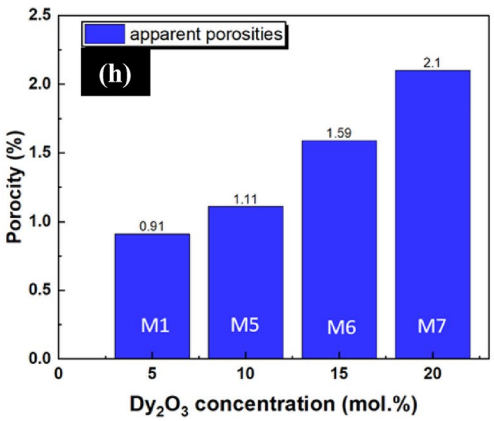

Fig. 5 continued

electronic properties. The FESEM results of the M1 pellet sample demonstrate that grain boundary defects in the crystal lattice can lead to a decrease in the electrical conductivity of ceramic materials, according to Qiannan Xue et al. [50]. The presence of neighboring crystals at the boundary inevitably leads to periodic changes in the atomic potential. These changes cause a potential barrier, leading to electron scattering. The extent of the barrier is closely associated with the grain boundary structure and the chemical bonding present [50]. Furthermore, previous studies have shown that incorporating anion vacancies may induce changes in the local geometric structure, significantly impacting the material's electrical performance. This phenomenon has been observed in the case of Vanadium-rich pellets [50, 51].

Including varied valence cations, such as DY^{3+} and V^{5+}, improves the stability of the Bi_2O_3 crystal structure and promotes the creation of oxygen vacancies. As the degree of substitution increases, the conductivity of ions also increases. This is because more oxygen voids are present in the material at higher substitution degrees. Incorporating mixed valence cations, such as DY^{3+} and V^{5+}, into the Bi_2O_3 crystal structure has been found to enhance its stability and promote the formation of oxygen vacancies. With an increase in substitution degree, the electrical and ionic conductivity of the material is observed to increase as a result of an increase in the number of oxygen vacancies. These findings suggest that introducing mixed valence cations can be a helpful strategy in enhancing the performance of Bi_2O_3-based materials for various applications, including solid oxide fuel cells and gas sensors. Figure 5h illustrates the apparent porosities of the sintered pellets M1, M5, M6, and M7, determined through the Archimedes drainage technique. The results indicate that the sintered pellets have a low level of void space, with an apparent porosity of no more than 2.5%. These findings are significant, as they suggest that the pellets possess desirable properties as a solid electrolyte for SOFCs. The observed increase in porosity can be attributed to the higher concentration of dysprosium because Dy_2O_3 has a higher melting point (~ 2330–2350 °C) than Bi_2O_3 (825 °C). The findings, in conjunction with the FESEM images depicted in Fig. 5, suggest that the sintered pellets exhibited sufficient density to satisfy the standards set for SOFC electrolytes, especially samples M1 and M2, and are well consistent with the results of the electrical measurements. Furthermore, the findings presented in this study align with the comparative densities displayed in Table 2 [52].

3.4 Electrical characteristics of the solid-state electrolytes

The graph presented in Fig. 6 displays the variation in electrical conductivity of disc-shaped samples with

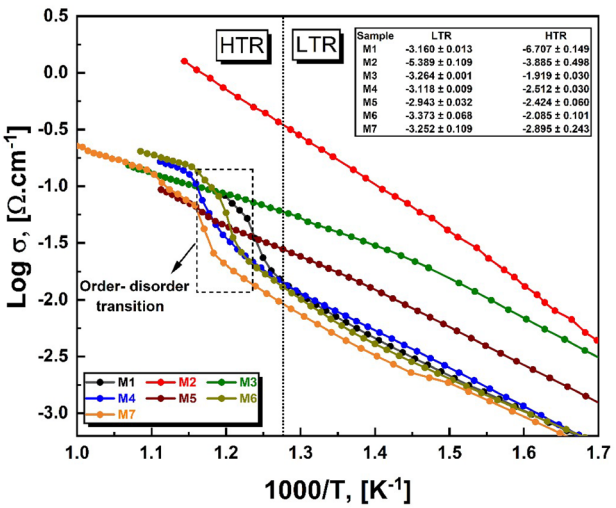

Fig. 6 The temperature dependence of electrical conductivity (σ) for $Bi_{1-x-y}V_xDy_yO_{1.5}$ ternary systems ($y = 0.05/x = 0.05$, 0.10, 0.15, 0.20, and $x = 0.05/y = 0.10$, 0.15, 0.20)

Table 2 The calculated theoretical, practical, and relative densities for the sintered samples

Composition	Theoretical densities(g/cm^3)	Practical densities (g/cm^3)	relative densities (%)	References
$Bi_{0.90}V_{0.05}Dy_{0.05}O_{1.5}$	8.771	8.672	96.981	8.487 [52]
$Bi_{0.85}V_{0.10}Dy_{0.05}O_{1.5}$	8.700	8.655	96.922	8.344 [52]
$Bi_{0.80}V_{0.15}Dy_{0.05}O_{1.5}$	8.770	8.701	95.875	8.637 [52]
$Bi_{0.75}V_{0.20}Dy_{0.05}O_{1.5}$	8.791	8.411	95.765	8.387 [52]
$Bi_{0.85}V_{0.05}Dy_{0.10}O_{1.5}$	8.729	8.342	95.777	This work
$Bi_{0.80}V_{0.05}Dy_{0.15}O_{1.5}$	8.782	8.433	98.487	This work
$Bi_{0.75}V_{0.05}Dy_{0.20}O_{1.5}$	8.796	8.444	95.399	This work

respect to temperature. The data in Fig. 6 indicates that the conductivity plots follow the Arrhenius equation. This equation is commonly represented as follows:

$$\sigma_T = \sigma_0 \exp\left(\frac{-E_a}{K_B T}\right), \quad (5)$$

where E_a is the activation energy associated with dc conductivity, σ_0 represents the pre-exponential factor, T denotes the temperature in K, and k_B stands for the Boltzmann constant.

The electrical conductivity of the pelletized samples increases proportionally with the rise in temperature due to the thermal activation of conducting species. In $Bi_{1-x-y}V_xD_yyO_{1.5}$ solid solutions, the primary source of electrical conduction is the defects present in the crystal lattice, such as vacant anion sites, vacancy accumulation, and interstitial aggregation. Numerous reports have conclusively demonstrated that the Arrhenius plot for doped metal oxide-based Bi_2O_3 exhibits the presence of two distinct regions [12, 15, 16, 23, 33]. The same trends were observed in conductivity graphs of ceramics M4, M6, and M7, as shown in Fig. 6. This is evidenced by a sharp increase in σ at approximately 710–723 °C. The literature attributes the phenomenon under consideration to the order-disorder transition (ODT), which is solely dependent on the particular configuration of oxygen in the crystal lattice [12, 15, 16]. This result is consistent with the obtained XRD analysis. Preceding the $\alpha \rightarrow \delta$ transition, the oxygen ions in the anion sublattice exhibit a random distribution within the structured tetrahedral sites (8c). During this transition, a certain fraction of the migratory O^{2-} ions tend to relocate to the octahedral positions (32f), characterized by a disordered structure and commonly referred to as the 32f Wyckoff position. This relocation results in the depletion of the 8c sites [53, 54]. Due to the low distance between empty ion positions in the surrounding sublattice, 32f positions are more dynamically promising for O^{2-} migration [32]. By comparison, the Arrhenius plots for the other ceramics (M2, M3, and M5) showed a linear variation of electrical conductivity over the temperature range. They demonstrated the conductivity variation as a function of V^{5+} and Dy^{3+} content over the entire temperature range, as shown in Fig. 6. These findings imply that $Bi_{0.85}V_{0.10}Dy_{0.05}O_{1.5}$ has the highest value of electrical conductivity. As observed in the V-rich ceramics, such as $Bi_{0.90}V_{0.05}Dy_{0.05}O_{1.5}$ and $Bi_{0.85}V_{0.10}Dy_{0.05}O_{1.5}$, the impact of polarizability on conductivity was seen. The observed samples demonstrated a range of electrical conductivities, varying from 0.123 to 0.965 $(\Omega\ cm)^{-1}$ when measured at 627 °C. On the other hand, ceramics exhibiting a more significant proportion of Dy exhibited diminished electrical conductivities, which spanned from 0.010 to 0.097 $(\Omega\ cm)^{-1}$ at a temperature of 627 °C. This implies that utilizing dopants with high polarizability is imperative to δ-phase stability and attain enhanced conductivity while minimizing the dopants' concentration. The results of the conductivity measurements are summarized in Table 3.

Table 3 demonstrates that sample M2 has the greatest ultimate conductivity of 0.964 $(\Omega.cm)^{-1}$ among all the synthesized samples. Hence, increased electrical conductivity is observed upon increasing V^{5+} concentration to 10%. When the Dy^{3+} and V^{5+} content is increased to 15%, there is a decrease in conductivity, as shown in Fig. 6. This decrease may be attributed to a reduction in the ratio of polarizable cations and

Table 3 Measured electrical conductivity and activation energies for samples that expert the order-disorder transition and those in the cubic *δ*-phase

Sample code	Composition	LTR (352–477 °C)			HTR (560–727 °C)			References
		Electrical conductivity σ $(\Omega\ cm)^{-1}$	Ea (eV)	Phase composition	Electrical conductivity $(\Omega\ cm)^{-1}$	Ea (eV)	Phase composition	
M1	$Bi_{0.90}V_{0.05}Dy_{0.05}O_{1.5}$	8.04×10^{-3}	1.340	$\alpha+\delta$	1.91×10^{-1}	1.286	δ	$\sigma = 1.97\times10^{-1}$ $(\Omega.cm)^{-1}$ at 750 °C [30]
M2	$Bi_{0.85}V_{0.10}Dy_{0.05}O_{1.5}$	6.20×10^{-1}	1.363	$\alpha+\delta$	9.65×10^{-1}	0.537	δ	
M3	$Bi_{0.80}V_{0.15}Dy_{0.05}O_{1.5}$	4.21×10^{-2}	1.528	$\alpha+\delta$	1.23×10^{-1}	0.551	δ	
M4	$Bi_{0.75}V_{0.20}Dy_{0.05}O_{1.5}$	8.94×10^{-3}	1.375	$\alpha+\delta$	1.65×10^{-1}	0.965	δ	$\sigma = 1.58\times10^{-1}$ $(\Omega.cm)^{-1}$ at 750 °C [29, 30]
M5	$Bi_{0.85}V_{0.05}Dy_{0.10}O_{1.5}$	1.89×10^{-2}	1.458	$\alpha+\delta$	9.75×10^{-2}	0.908	δ	
M6	$Bi_{0.80}V_{0.05}Dy_{0.15}O_{1.5}$	7.80×10^{-3}	1.211	$\alpha+\delta$	1.14×10^{-3}	1.139	δ	
M7	$Bi_{0.75}V_{0.05}Dy_{0.20}O_{1.5}$	5.18×10^{-3}	1.267	$\alpha+\delta$	1.04×10^{-3}	1.129	δ	

the number of oxide ion vacancies. The observed phenomenon in this particular instance can be ascribed to the fact that the ionic radii of the dopant materials are comparatively smaller in size compared to Bi_2O_3. We have chosen early studies concentrating on double-doped research of Dy_2O_3 and Sm_2O_3-based Bi_2O_3 reported by M. Kş et al. to construct a comparison analysis with existing literature [29]. In this study, Kış et al. demonstrated that the electrical conductivity of fluorite-type phases in Dy_2O_3 and Sm_2O_3 double-doped Bi_2O_3-based compositions at a temperature of 750 °C ranges from 9.89×10^{-3} to 2.50×10^{-2} $(\Omega\ cm)^{-1}$. According to M. Kış et al. [29], it was observed that the conductivity of δ-Bi_2O_3 phases, when doped with Dy_2O_3, exhibited a positive correlation with temperature. Furthermore, a significant increase in conductivity was observed after reaching a temperature of approximately 750 °C, suggesting the occurrence of δ-phase formation. The obtained conductivity level is comparable to the double-doping approach elucidated by D.W. Jung et al. [23], demonstrating the most effective strategy for achieving optimal conductivity. Table 3 presents the electrical activation energies (E_a) for two specific temperature ranges: low-temperature (LTR) and high-temperature (HTR). In theory, the ODT enables the occurrence of two separate conductivity pathways on the linear curve, forming LTR and HTR [55]. The sublattice, arranged in a specific order (i.e., LTR), has a notable activation energy (E_a) level. The sublattice that lacks specific order due to the $\alpha \rightarrow \delta$ transition definitely exhibits comparatively lower activation energy. Furthermore, the transition from order to disorder is unequivocally restricted by substantial double doping, leading to a noticeable decrease in the inequality between the activation energies of LTR and HTR as the dopant concentration rises. According to A.G. Jolley et al., it has been noted that Bi_2O_3-based systems that are doped with a large number of dopants have a greater inclination to contain an ordered anion sublattice rather than a disordered sublattice. This phenomenon has been found to result in a reduction in total conductivity [56]. The E_a values were determined by fitting a line to the conductivity curves in two temperature ranges. Based on the data presented in Table 3, it is apparent that the XRD pattern of sample M2 has the characteristic peaks associated with a stabilized δ-phase. This sample has a minimum activation energy of 0.537 eV, consistent with the activation energy estimated by Y. Polat et al. [30]. According to theoretical postulations, the polarizability of a cation exhibits a direct proportionality to the cube of its radius. This implies that cations with greater radii, such as La, possess a higher degree of polarizability than their smaller counterparts [57]. The activation energy of the prepared samples shows a variation between 1.211 and 1.528 eV in LTR. Similarly, this variation is also observed in the HTR, falling within the range of 0.537–1.286 eV [29, 30, 33]. Utilizing dopants with high polarizability to stabilize the cubic δ-phase can result in optimal conductivity for doped Bi_2O_3 crystalline solids with minimal dopant usage.

A comprehensive assessment was conducted to evaluate the applicability of electrochemical impedance spectroscopy (EIS) within the frequency range of 1 Hz to 10 kHz to provide a thorough investigation of the operational efficiency of the designed electrolytic fuel cell. The Nyquist and Bode plots are displayed in Figs. 7 and 8 indicate a significant improvement in cell performance due to the doping process. The Nyquist plots were thoroughly analyzed and employed to estimate the equivalent circuit. It is worth noting that the increase in vanadium concentration within the samples (M1-M4) exhibited distinct electrochemical impedance spectroscopy (EIS) features, especially the sample M2. This sample showed the lowest ohmic resistance at high frequency in the Nyquist plot, corresponding to the largest recorded grain size observed from high-resolution scanning electron microscopy (HRSEM) and the highest electrical conductivity measurements. These findings are presented in Table 4. The grain growth in sample M2 ($Bi_{0.85}V_{0.10}Dy_{0.05}O_{1.5}$) decreased the grain boundary contribution to the total resistance. It facilitated the charge transfer between grains, hence decreasing the charge transfer resistance (R_2) at the electrode/electrolyte interface and yielding better conductivity. This indicates the occurrence of mass transport/diffusion phenomena, specifically, the oxygen concentration distribution at the cathode [58]. Additionally, at this concentration of vanadium, a stable constant plateau was observed with the lowest impedance and phase angle, as depicted in Bode plots shown in Fig. 8, dominating the ohmic conduction. In the intermediate frequency region, the capacitive contribution dominated the ohmic current [59, 60]. The composition $Bi_{0.85}V_{0.10}Dy_{0.05}O_{1.5}$ demonstrated the lowest phase angle, impedance, and f_{max} (70 Hz) compared to the other fabricated ceramics. Including vanadium at a concentration of 10% has been demonstrated to validate the enhanced electrochemical

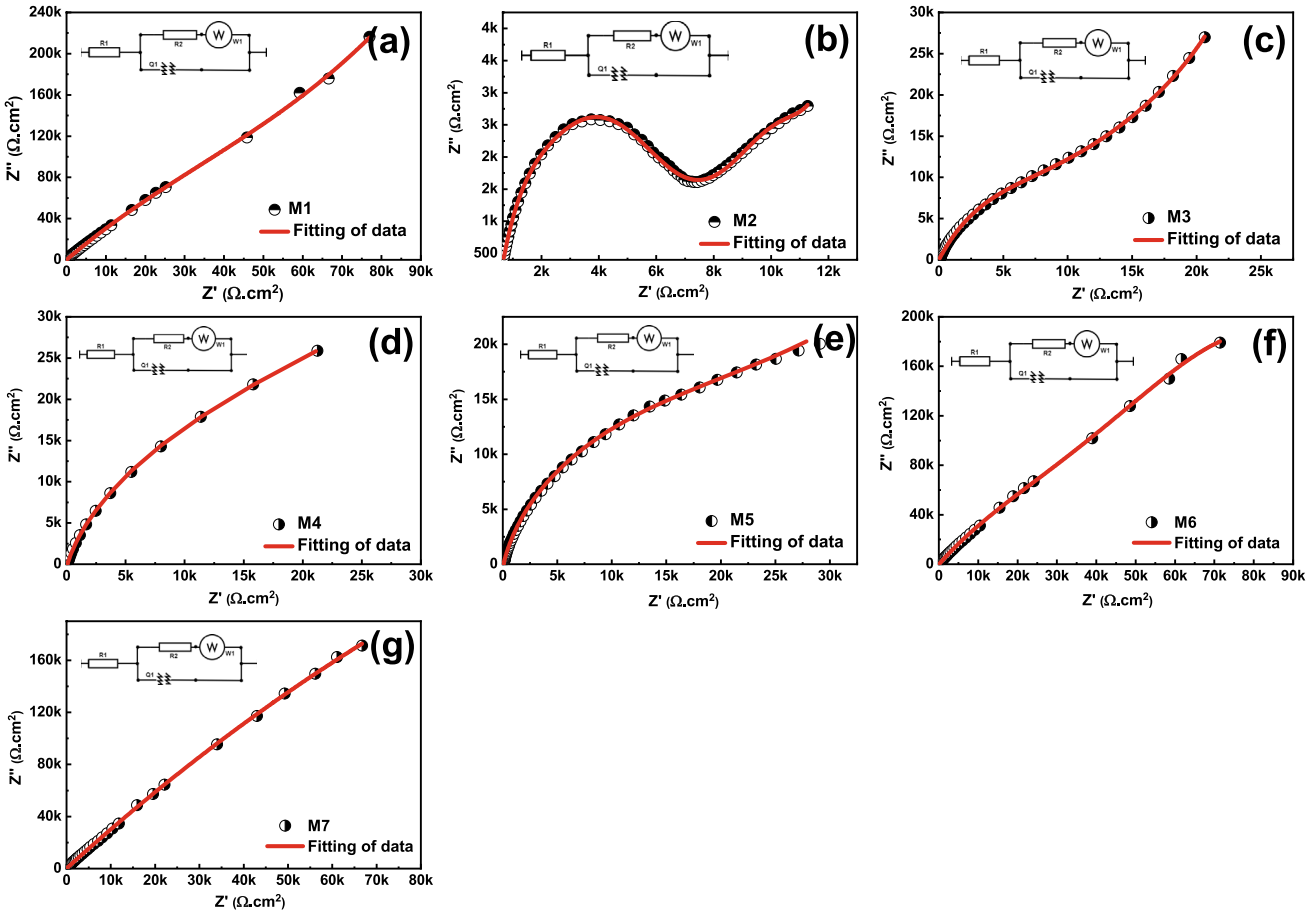

Fig. 7 a–g Nyquist plot showing the solid lines representing the fittings of stabilized δ-phase $Bi_{1-x-y}V_xDy_yO_{1.5}$ ceramics, ($y = 0.05/x = 0.05$, 0.10, 0.15, 0.20, and $x = 0.05/y = 0.10$, 0.15, 0.20). The inset shows the equivalent circuit diagram

performance of the fuel cell design [61]. On the other side, the addition of Dysprosium with different concentrations induced the formation of oxygen deficiencies, resulting in the formation of pores as revealed in the HRSEM, which play a significant role in trapping the charge transport, yielding a high impedance as revealed in Nyquist and Bode plots. Then, it can be concluded that the increment of Dy^{3+}-concentration in the Dy^{3+}–V^{5+} double-doping approach could negatively affect the performance of the developed cells. Total internal resistance (R_S) may be found as the intercept of the semicircle on the real axis in the high-frequency zone; charge transfer resistance (R_2) is shown by the narrow arc [33]. Figure 7a–g displays the Nyquist graphs of the constructed cells using the various solid electrolyte solution and their corresponding equivalent circuits. A low R_2 value indicates that quicker ion conduction increases throughout charging and discharging. The $Bi_{0.85}V_{0.10}Dy_{0.05}O_{1.5}$ solid electrolyte had the lowest R_2 value of 700 Ω compared to other compositions. Each fabricated cell exhibited a concave semicircular shape with a line running diagonally in the low-frequency range, indicating the occurrence of mass transport/diffusion phenomena, specifically, the oxygen concentration distribution at the cathode [58]. Table 4 shows the retrieved circuit equivalent parameters. The ohmic series resistance (R_1) encompasses the combined effects of the bipolar electrodes and the bulk polarization resistance. The charge transport resistance (R_2) value is determined by the rate at which the electrode reaction takes place. The Warburg element (W_1) represents vanadium diffusion characteristics and is included with the constant phase element (Q). The electrode resistance decreases with increasing catalytic functions [59, 60].

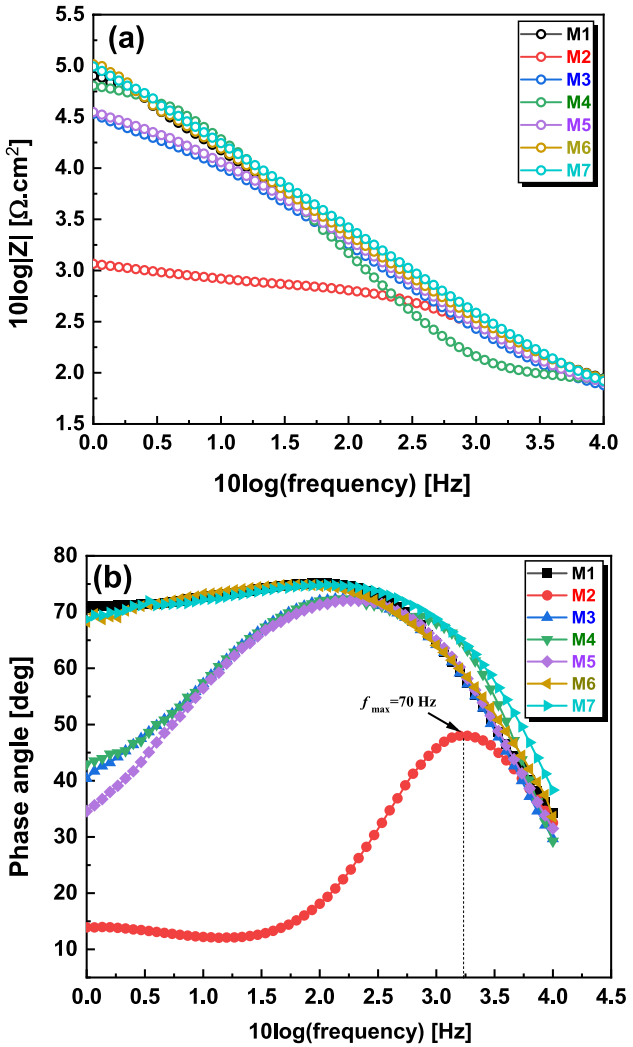

Fig. 8 Bode plots: **a** 10log |Z| vs. 10log *f*, **b** phase angle vs. 10log *f*, of the impedance spectra of the stabilized *δ*-phase $Bi_{1-x-y}V_xDy_yO_{1.5}$ ceramics, ($y=0.05/x=0.05$, 0.10, 0.15, 0.20, and $x=0.05/y=0.10$, 0.15, 0.20)

4 Conclusion

The Dy-V co-doped Bi_2O_3 was synthesized under atmospheric conditions using the solid-state approach. The impact of rare-earth cations as dopants on the phase stability of δ–Bi_2O_3 is crucial, especially in Dy-rich and V-rich ceramics, as indicated by the XRD profiles. The observed diffraction peaks on the XRD patterns suggest a mixed crystallographic phase, which gradually diminishes with increased mutual dopant concentrations. This implies a transition to the single fcc δ-phase. The Rietveld analysis and electron density representation indicate the absence of impure peaks from *α*-Bi_2O_3, emphasizing the transition to the δ-phase polymorphs. An increase in the dopant ratio causes a noticeable shift toward higher 2θ in the sharp peaks associated with the (111) plane. This shift strongly suggests a significant alteration in the lattice characteristics. In the DTA curves for samples M4 and M7, a distinct endothermic peak is observed at temperatures of approximately 724.5 and 744.5 °C. These peaks indicate a phase transition from the monoclinic *α*-phase to the cubic *δ*-phase. The endothermic peaks are also attributed to an order-disorder transition (ODT), which signifies a positional migration of O^{2-} ions in the oxygen sublattice of the doped crystal structure rather than a likely phase transition. Based on the conductivity measurements and EIS analysis, $Bi_{0.85}V_{0.10}Dy_{0.05}O_{1.5}$ exhibits the highest electrical conductivity despite being in the mixed phase, with an outstanding value of 0.965 $(\Omega\ cm)^{-1}$ and an optimal activation energy of 0.537 eV at 627 °C. This exceptional performance is attributed to the high polarizability and mixed valence cations, especially in V^{5+}-rich ceramics, compared to the Dy^{3+}-rich compositions with a reduced conductivity of 0.010 to 0.097 $(\Omega\ cm)^{-1}$. The presence of mixed valence cations with different ionic radii and concentrations further stimulates the formation of oxygen vacancies in the crystal lattice of Bi (III) oxide. It

Table 4 The circuit equivalent parameters derived from EIS measurements

Sample code	Ceramic	R_1 (Ω)	R_2 ($\times10^4$ Ω)	W_1 ($\times10^{-6}$ Ω. $Hz^{-1/2}$)	Q_1 ($\times10^{-6}$ S^N/Ω)	N_1
M1	$Bi_{0.90}V_{0.05}Dy_{0.05}O_{1.5}$	66.60	0.78	3520	1.77	0.859
M2	$Bi_{0.85}V_{0.10}Dy_{0.05}O_{1.5}$	50.34	0.07	755.4	2.77	0.810
M3	$Bi_{0.80}V_{0.15}Dy_{0.05}O_{1.5}$	59.61	1.55	11.21	2.03	0.865
M4	$Bi_{0.75}V_{0.20}Dy_{0.05}O_{1.5}$	71.72	3.98	9.428	1.94	0.865
M5	$Bi_{0.85}V_{0.05}Dy_{0.10}O_{1.5}$	60.12	2.69	18.95	2.06	0.851
M6	$Bi_{0.80}V_{0.05}Dy_{0.15}O_{1.5}$	74.28	92.8	3077	1.64	0.864
M7	$Bi_{0.75}V_{0.05}Dy_{0.20}O_{1.5}$	54.33	97.4	9690	1.49	0.857

enhances the thermal stability of compositions, promoting the sample's superior conductivity. The V^{5+}–Dy^{3+} double-doped Bi_2O_3 systems are highly promising as solid electrolytes for SOFCs, owing to their high oxygen ion conductivity and remarkable structural stability. The FESEM micrographs of pellet sample M2 demonstrate the absence of any pore development, confirming a remarkably high degree of densification and significantly enhancing electrical and electrochemical performance. In comparison, incorporating Dy^{3+} leads to the formation of the pores. Observing increased pore formation of the as-sintered samples is a critical and concrete indication of the successful formation of densely packed pellets. This requirement is crucial for intermediate-temperature SOFCs. According to the Nyquist plots data, it is evident that the impedance drops with the increase in vanadium doping level until it reaches $Bi_{0.85}V_{0.10}Dy_{0.05}O_{1.5}$. Further, as the dysprosium content increases, the impedance rises, leading to a decline in cell performance.

Acknowledgements

The authors of this study wish to express their sincere gratitude to the laboratory staff at the Physics Department, Aliraqia University, Iraq, for their invaluable assistance. Additionally, we extend our heartfelt appreciation to Dr. Ahmed Elmahalawy, a respected member of the physics department at the Faculty of Science—Suez Canal University, for his generous support and guidance.

Author contributions

Ahmed H. Ibrahim: conceptualization, methodology, investigation, formal analysis, data curation, software, visualization, data analysis, initial manuscript draft, and review. Yehia M. Abbas: supervision, experimental characterizations, manuscript review and editing. Marwa H. Ali& H.A.Ayoub: data validation, manuscript review, and editing. Mustafa Aldoori: investigation, funding, data analysis, reviewing, and editing. All authors have participated in the conception, analysis, and interpretation of the data. The authors have participated in revising it critically for important intellectual content and approval of the final version.

Funding

Open access funding provided by The Science, Technology & Innovation Funding Authority (STDF) in cooperation with The Egyptian Knowledge Bank (EKB). There is no funding from any agents.

Data availability

All authors declare the data at the heart of the research article is the authors' original data; these data haven't received prior publication and aren't under consideration for publication elsewhere.

Declarations

Conflict of interest The author(s) declared no potential conflicts of interest with respect to the research, authorship, and publication of this article. All authors declare that they have no conflicts of interest, and the article is the author's original work, has not received prior publication, and isn't under consideration for publication elsewhere. We are stating that this manuscript has not been submitted to, nor is it under review at, another journal or other publishing venue. Also, the authors have no affiliation with any organization with a direct or indirect financial interest in the subject matter discussed in the manuscript.

Ethical approval This manuscript is the author's original work, which has not been previously published elsewhere, and compliance with ethical standards. All sources used are properly disclosed, and all authors have been personally and actively involved in substantial work leading to this paper.

Supplementary Information The online version contains supplementary material available at https://doi.org/10.1007/s10854-024-12371-4.

References

1. A. Fedotov, V. Shendyukov, L. Tsybulskaya, S. Perevoznikov, M. Dong, X. Xue, X. Feng, M.I. Sayyed, T. Zubar, A. Trukhanov, D. Tishkevich, Electrodeposition conditions-dependent crystal structure, morphology and electronic properties of Bi films. J. Alloys Compd. **887**, 161451 (2021). https://doi.org/10.1016/j.jallcom.2021.161451
2. M. Han, X. Tang, H. Yin, S. Peng, Fabrication, microstructure, and properties of a YSZ electrolyte for SOFCs. J. Power Sources **165**(2), 757–763 (2007)
3. Y.L. Liu, A. Hagen, R. Barfod, M. Chen, H.J. Wang, F.W. Poulsen, P.V. Hendriksen, Microstructural studies on degradation of interface between LSM–YSZ cathode and YSZ electrolyte in SOFCs. Solid State Ion **180**, 1298–1304 (2009). https://doi.org/10.1016/j.ssi.2009.07.011
4. E.D. Wachsman, K.T. Lee, Lowering the temperature of solid oxide fuel cells. Science. **334**, 935–939 (2011). https://doi.org/10.1126/science.1204090
5. Z. Zakaria, Z. Awang Mat, S.H. Abu Hassan, Y. Boon Kar, A review of solid oxide fuel cell component fabrication methods toward lowering temperature. Int. J. Energy Res. **44**(2), 594–611 (2020). https://doi.org/10.1002/er.4907
6. H.A. Harwig, A.G. Gerards, The polymorphism of bismuth sesquioxide. Thermochim. Acta **28**, 121–131 (1979). https://doi.org/10.1016/0040-6031(79)87011-2
7. R.D. Bayliss, S.N. Cook, S. Kotsantonis, R.J. Chater, J.A. Kilner, Oxygen ion diffusion and surface exchange properties of the α- and δ-phases of Bi_2O_3. Adv. Energy Mater. **4**, 1301575 (2014). https://doi.org/10.1002/aenm.201301575
8. S. Boyapati, E.D. Wachsman, N. Jiang, Effect of oxygen sublattice ordering on interstitial transport mechanism and conductivity activation energies in phase-stabilized cubic bismuth oxides. Solid State Ionics. **140**, 149–160 (2001). https://doi.org/10.1016/S0167-2738(01)00698-1
9. X. Li, X. Kuang, J. Sun, Rare earth elements-based oxide ion conductors. Inorg. Chem. Front. **8**, 1374–1398 (2021). https://doi.org/10.1039/D0QI00848F
10. P. Temluxame, N. Laosiripojana, S. Assabumrungrat, P. Puengjinda, P. Kim-, Lohsoontorn, Phase transformation and electrical properties of bismuth oxide doped scandium cerium and gadolinium stabilized zirconia ($0.5Gd_{0.5}Ce_{10}ScSZ$) for solid oxide electrolysis cell. Int. J. Hydrog Energy. **45**(55), 29953–29965 (2020). https://doi.org/10.1016/j.ijhydene.2020.08.085
11. S. Cobaner, S. Yilmaz, Electrical and structural properties of new type Er and Yb doped bismuth oxide solid electrolytes synthesized by Pechini method. J. Electro Ceram. **137**, 83–92 (2021). https://doi.org/10.1007/s10832-021-00248-5
12. S. Yilmaz, B. Kavici, C. Celen, E. Yildiz, A. Gurbuz, Structure and conductivity characterization of new type ionic conductor stabilized bismuth oxide ternary systems. Chin. J. Phys. **56**, 362–373 (2018). https://doi.org/10.1016/j.cjph.2017.11.010
13. Y.S. Ayhan, A. Buyukaksoy, Impact of fabrication temperature on the stability of yttria doped bismuth oxide ceramics. Solid State Ion **338**, 66–73 (2019).
14. S. Bandyopadhyay, A. Dutta, A structural insight into the electrical properties of Dy–Ho co–doped phase stabilized bismuth oxide based electrolytes. J. Electroanal. Chem. **817**, 55–64 (2018). https://doi.org/10.1016/j.jelechem.2018.03.063
15. T.K. Pietrzak, J.E. Garbarczyk, M. Wasiucionek, Stabilization of the δ–Bi_2O_3–like structure down to room temperature by thermal nano crystallization of bismuth oxide–based glasses. Solid State Ion. **323**, 78–84 (2018). https://doi.org/10.1016/j. ssi.2018.05.021
16. X. Wang, W. Zhou, J.B. DeLisio, G.C. Egan, M.R. Zachariah, Doped δ–bismuth oxides to investigate oxygen ion transport as a metric for condensed phase thermite ignition. Phys. Chem. Chem. Phys. **19**(20), 12749–12758 (2017). https://doi.org/10.1039/C6CP08532F
17. H.O. Torun, S. Çakar, Thermal characterization of Er–doped and Er–Gd co–doped ceria–based electrolyte materials for SOFC. J. Therm. Anal. Calorim. **133**, 1233–1239 (2018). https://doi.org/10.1007/s10973-018-7189
18. A.V. Trukhanov, V.A. Turchenko, V.G. Kostishin, F. Damay, F. Porcher, N. Lupu, B. Bozzo, I. Fina, S. Polosan, M.V. Silibin, M.M. Salem, D.I. Tishkevich, S.V. Trukhanov, The origin of the dual ferroic properties in quasi-centrosymmetrical SrFe12–*x*In*x*O19 hexaferrites. J. Alloys

Compd. **886**, 161249 (2021). https://doi.org/10.1016/j.jallcom.2021.161249

19. D.S. Aidhy, J.C. Nino, S.B. Sinnott, E.D. Wachsman, S.R. Phillpot, Vacancy-ordered structure of cubic bismuth oxide from simulation and crystallographic analysis. J. Am. Ceram. Soc. **91**(7), 2349–2356 (2008). https://doi.org/10.1111/j.15512916.2008.02463.x
20. D. Tishkevich, A. Vorobjova, D. Shimanovich, E. Kaniukov, A. Kozlovskiy, M. Zdorovets, D. Vinnik, A. Turutin, I. Kubasov, A. Kislyuk et al., Magnetic properties of the densely packed ultra-long Ni nanowires encapsulated in alumina membrane. Nanomaterials **11**, 1775 (2021). https://doi.org/10.3390/nano11071775
21. A. Vorobjova, D. Tishkevich, D. Shimanovich, T. Zubar, K. Astapovich, A. Kozlovskiy, M. Zdorovets, A. Zhaludkevich, D. Lyakhov, D. Michels, D. Vinnik, V. Fedosyuk, A. Trukhanov, The influence of the synthesis conditions on the magnetic behaviour of the densely packed arrays of Ni nanowires in porous anodic alumina membranes RSC Adv. **11**, 3952–3962 (2021). https://doi.org/10.1039/D0RA07529A
22. D.L. Shimanovich, A.I. Vorobjova, D.I. Tishkevich, A.V. Trukhanov, M.V. Zdorovets, A.L. Kozlovskiy, Beilstein J. Nanotechnol. **9**, 1423–1436 (2018). https://doi.org/10.3762/bjnano.9.135
23. D.W. Jung, K.L. Duncan, E.D. Wachsman, Effect of total dopant concentration and dopant ratio on conductivity of $(DyO_{1.5})_x$–$(WO_3)_y$–$(BiO_{1.5})_{1-x-y}$. Acta Mater. **58**, 355–363 (2010). https://doi.org/10.1016/j.actamat.2009.08.072
24. D.W. Jung, K.T. Lee, E.D. Wachsman, Dysprosium and gadolinium double doped bismuth oxide electrolytes for low temperature solid oxide fuel cells. J. Electrochem. Soc. **163**, 411 (2016). https://doi.org/10.1149/2.0951605jes
25. S.E. Lin, W.C.J. Wei, Long-term degradation of Ta_2O_5-doped Bi_2O_3 systems J. Eur. Ceram. Soc. **31**, 3081–3086 (2011). https://doi.org/10.1016/j.jeurceramsoc.2011.04.015
26. S. Yilmaz, O. Turkoglu, I. Belenli, Measurement and properties of the oxide ionic conductivity of β-phase in the binary system of (Bi2O3)1−*x*(Sm2O3)*x*. Mater. Chem. Phys. **112**, 472–477 (2008). https://doi.org/10.1016/j.matchemphys.2008.06.002
27. R. Punia, R.S. Kundu, J. Hooda, S. Dhankhar, S. Dahiya, N. Kishore, Effect of Bi_2O_3 on structural, optical, and other physical properties of semiconducting zinc vanadate glasses. J. Appl. Phys. **110**, 33527–33533 (2011). https://doi.org/10.1063/1.3621188
28. I. Abrahams, F. Krok, A model for the mechanism of low temperature ionic conduction in divalent-substituted γ-BIMEVOXes. Solid State Ion. **157**, 139–145 (2003). https://doi.org/10.1016/S0167-2738(02)00201-1
29. M. Kış, M. Arı, Y. Polat, B. Erdoğan, T. Karaaslan, Structural and temperature dependent electrical conductivity properties of Dy_2O_3-Sm_2O_3 co-doped Bi_2O_3. J. Struct. Chem. **59**, 1133–1140 (2018). https://doi.org/10.1134/S0022476618050165
30. Y. Polat, M. Arı, Y. Dağdemir, Phase stability, thermal, electrical, and structural properties of $(Bi_2O_3)_{1-x-y}(Sm_2O_3)_x(CeO_2)_y$ electrolytes for solid oxide fuel cells. Ph. Transit. **90**, 387–398 (2017). https://doi.org/10.1080/01411594.2016.1206899
31. S. Khan, K. Singh, Effect of MgO on structural, thermal, and conducting properties of $V_{2-X}MgXO_{5-\delta}$ (x = 0.05 – 0.30) systems. Ceram. Int. **45**, 695–701 (2019). https://doi.org/10.1016/j.ceramint.2018.09.231
32. M. Yashima, D. Ishimura, Crystal structure and disorder of the fast oxide-ion conductor cubic Bi_2O_3. Chem. Phys. Lett. **378**(3–4), 395 (2003)
33. A.H. Ibrahim, Y.M. Abbas, H.A. Ayoub, M.H. Ali, M. Aldoori, Novel synthesis of stabilized $Bi_{1-x-y}Gd_xDy_yO_{1.5}$ solid electrolytes with enhanced conductivity for intermediate temperature solid oxide fuel cells (SOFCs). J. Rare Earths (2023). https://doi.org/10.1016/j.jre.2023.10.003
34. A.H. Harwig, A.G. Gerards, On the structure of bismuth sesquioxide, the α, β, γ and δ-phase. Chem. **444**(1–2), 151 (1978)
35. B.T.M. Willis, The anomalous behavior of the neutron reflex ion of fluorite. Acta Cryst. **18**(1), 75 (1965)
36. S. Boyapati, E.D. Wachsman, B.C. Chakoumakos, Neutron diffraction study of occupancy and positional order of oxygen ions in phase stabilized cubic bismuth oxides. Solid State Ionics. **138**(3–4), 293 (2001)
37. S. Arasteh, A. Maghsoudipour, M. Alizadeh, A. Nemati, Effect of Y_2O_3 and Er_2O_3 co-dopants on phase stabilization of bismuth oxide. Ceram. Int. **37**(8), 3451 (2011)
38. L. Gui, Y. Ling, G. Li, Z. Wang, Y. Wan, R. Wang, B. He, L. Zhao, Enhanced sinter ability and conductivity of $BaZr_{0.3}Ce_{0.5}Y_{0.2}O_{3-\delta}$ by addition of bismuth oxide for proton conducting solid oxide fuel cells. J. Power Sources. **301**, 369–375 (2016).
39. S. Koçyiğit, Boron, and praseodymium doped bismuth oxide nanocomposites: preparation and sintering effects. J. Alloys Compd. **740**, 941–948 (2018). https://doi.org/10.1016/j.jallcom.2018.01.020
40. G.O. Hernandez, J.O. Flores, C.P. Vargas, J.E. Alfonso, E.R. Parrae, Structural, chemical, and electrochemical studies of bismuth oxide thin films growth via unbalanced magnetron sputtering. Surf. Interfaces. **21**, 100627 (2020). https://doi.org/10.1016/j.surfin.2020.100627

41. S. Gupta, R. Singh, M.D. Anoop, V. Kulshrestha, D.N. Srivastava, K. Ray, S.L. Kothari, K. Awasthi, M. Kumar, Electrochemical sensor for detection of mercury (II) ions in water using nanostructured bismuth hexagons. Appl. Phys. A **124**, 737 (2018). https://doi.org/10.1007/s00339-018-2161-9
42. G.-H. Jiang, X. Li, Z. Wei, T.-T. Jiang, X.-X. Du, W.-X. Chen, Effects of N and/or S doping on structure and photocatalytic properties of BiOBr crystals. Acta Metall. Sin **28**, 460–466 (2015). https://doi.org/10.1007/s40195-015-0220-1
43. D. Wang, G. He, Z. Fang, L. Hao, Z. Sun, Y. Liu, Interface chemistry modulation and dielectric optimization of TMA-passivated HfDyOx/Ge gate stacks using doping concentration and thermal treatment. RSC Adv. **10**(2), 938–951 (2020). https://doi.org/10.1039/c9ra08335a
44. G. Silversmit, D. Depla, H. Poelman, G.B. Marin, R. De Gryse, J. Electron. Spectrosc. Relat. Phenom. **135**, 167 (2004)
45. A. Garcia, N. Yan, A. Vincent, A. Singh, J.M. Hill, K.T. Chuang, J.-L. Luo, Highly cost-effective and sulfur/coking resistant VOx-grafted TiO_2 nanoparticles as an efficient anode catalyst for direct conversion of dry sour methane in solid oxide fuel cells. J. Mater. Chem. A **3**(47), 23973–23980 (2015). https://doi.org/10.1039/c5ta06453h
46. B. Oprea, T. Radu, S. Simon, XPS investigation of atomic environment changes on surface of B_2O_3–Bi_2O_3 glasses. J. Non-Cryst Solids. **379**, 35–39 (2013). https://doi.org/10.1016/j.jnoncrysol.2013.07.024
47. I.N. Reddy, C.V. Reddy, M. Cho, J. Shim, D. Kim, Structural, optical and XPS study of thermal evaporated In_2O_3 thin films. Mater. Res. Express. **4**(8), 086406 (2017). https://doi.org/10.1088/2053-1591/aa7f59
48. K.R. Kendall, C. Navas, J.K. Thomas, H.C. Zur Loye, Recent developments in oxide ion conductors: aurivillius phases. Chem. Mater. **8**, 642–649 (1996)
49. S. Durmus, V. Çorumlu, T. Çifci, I. Ermis, M. Arı, Electrical structural and thermal properties of nanoceramic $(Bi_2O_3)_{1-x-y}(Ho_2O_3)_x(Tm_2O_3)$y ternary system. Ceram. Int. **39**, 5241 (2013)
50. Q. Xue, X. Huang, J. Zhang, H. Zhang, Z. Feng, Grain boundary segregation and its influences on ionic conduction properties of scandia doped zirconia electrolytes. J. Rare Earths. **37**(6), 645 (2019)
51. H. Bishara, S. Lee, T. Brink, M. Ghidelli, G. Dehm, Understanding grain boundary electrical resistivity in Cu: the effect of boundary structure. ACS Nano **15**(10), 16607 (2021)
52. Y. Gao, M. Zhong, J. Chen, S. Wang, B. Zhang, Q. Li, W. Liu, J.-T. Gao, C.-X. Li, C.-J. Li, Stabilities and performance of single cubic phase dysprosium and zirconium co-doped bismuth oxide electrolytes for low temperature solid oxide fuel cells. Mater. Adv. **4**(13), 2839–2852 (2023).
53. N. Jiang, E.D. Wachsman, Structural stability, and conductivity of phase–stabilized cubic bismuth oxides. J. Am. Ceram. Soc. **82**, 57–64 (2004).
54. E.D. Wachsman, S. Boyapati, N. Jiang, Effect of dopant polarizability on oxygen sublattice order in phase–stabilized cubic bismuth oxides. Ionics. **7**, 1–6 (2001). https://doi.org/10.1007/BF02375460
55. W. Fang, T. Yang, K. Huang, In situ synthesis of a high–performance bismuth oxide based composite cathode for low temperature solid oxide fuel cells. Chem. Commun. **55**, 2801–2804 (2019). https://doi.org/10.1039/C9CC00442D
56. A.G. Jolley, E.D. Wachsman, A new double doped bismuth oxide with stable ionic conductivity at intermediate temperatures. ECS Trans. **78**(1), 355–360 (2017)
57. R. Bhattacharyya, S. Das, S. Omar, High ionic conductivity of Mg^{2+}–doped non–stoichiometric sodium bismuth titanate. Acta Mater. **159**, 8–15 (2018). https://doi.org/10.1016/j. actamat.2018.08.007
58. I. Pivac, B. Šimić, F. Barbir, Experimental diagnostics and modeling of inductive phenomena at low frequencies in impedance spectra of proton exchange membrane fuel cells. J. Power Sources. **365**, 240–248 (2017). https://doi.org/10.1016/j.jpowsour.2017.08.087
59. N. Shaheen, Z. Chen, Y. Nong, T. Su, M. Yousaf, Y. Lu, L. Li, Enhancing ORR Catalytic activity and electrochemical investigation of $La_{1-2x}Ba_xBi_xFeO_3$ cathode for low-temperature solid oxide fuel cell. Crystals **13**, 822 (2023). https://doi.org/10.3390/cryst13050822
60. B. Najafi, P. Bonomi, A. Casalegno, F. Rinaldi, A. Baricci, Rapid fault diagnosis of PEM fuel cells through optimal electrochemical impedance spectroscopy tests. Energies **13**, 3643 (2020). https://doi.org/10.3390/en13143643
61. J. Song, T. Zhu, X. Chen, W. Ni, Q. Zhong, Cobalt and titanium substituted $SrFeO_3$ based perovskite as efficient symmetrical electrode for solid oxide fuel cell. J. Materiomics **6**(2), 377 (2020). https://doi.org/10.1016/j.jmat.2020.02.009